# Magnetic stability against calcining of microwave-synthesized $CoFe_2O_4$ nanoparticles

**Elena Bartolomé *[a], Pablo Cayado [b], Eduardo Solano [c], Susagna Ricart [b], Jaume Gázquez [b], Bernat Mundet [b], Mariona Coll [b],Teresa Puig [b], Xavier Obradors [b], Manuel Valvidares [d], Javier Herrero-Martín [d], Pierlugi Gargiani [d] and Eric Pellegrin [d]**

[a]*Escola Universitària Salesiana de Sarrià (EUSS), Passeig Sant Joan Bosco, 74, 08710 Barcelona, Spain. E-mail: ebartolome@euss.es*

[b]*Institut de Ciència de Materials de Barcelona, Spain*

[c]*Department of Solid State Sciences, Faculty of Sciences, Ghent University, Krijgslaan 281/S1, 9000 Ghent, Belgium*

[d]*ALBA Synchrotron Light Source, Barcelona, Spain*

---

High quality $CoFe_2O_4$ nanoparticles were synthesized using a one-pot, microwave assisted method, that allows forming stable colloidal solutions in alcoholic solvents, as required for the preparation by Chemical Solution Deposition of hybrid nanocomposite ferromagnetic-high $T_c$ $YBa_2Cu_3O_7$ superconducting films or devices. We have investigated how the thermal process necessary for the preparation of such epitaxial nanocomposites, involving high temperatures (800 °C) and oxygen partial pressures (1 atm), affects the structure and magnetic properties of the isolated nanoparticles. The NPs were fully characterised by XRD, SQUID, STEM-EELS and XMCD at four different stages of the thermal process. Results show that, despite intermediate changes in the cation distribution occur during the process, the final NP magnetization is stable against the thermal treatment. This result opens up perspectives for the preparation of hybrid YBCO films with embedded magnetic NPs using low-cost chemical-solution methods.

---

## Introduction

Cobalt ferrite (CoFe2O4) nanoparticles, generally presenting a high magnetic anisotropy, are of high technological interest for application in electronic devices,1 high density magnetic recording,2 contrast agents in medical resonance imaging,3 gas sensors4etc… This has motivated the development of many different methods for the synthesis of CoFe2O4 nanoparticles (NPs), including hydrothermal methods,5,6 sol–gel

processes,7 co-precipitation,8,9 solvothermal decomposition10,11etc. By using these techniques, nanocrystals with different morphologies, such as cubes,5,12 spheres,5,6 and pseudospheres,13 have been obtained. Iron(III) reducing bacterium has also been utilized for the extracellular production of NPs.14 Recently, a novel one-pot synthesis method for $CoFe_2O_4$ NPs from bimetallic pivalate clusters as single-source precursors has been reported.15

At present, $CoFe_2O_4$ NPs are considered good potential candidates for the fabrication of hybrid, high Tc superconductor–ferromagnetic nanocomposites. It has already been shown that the incorporation of non-magnetic secondary phases into $YBa_2Cu_3O_7$ (YBCO) strongly increases the vortex pinning efficiency,16,17 ultimately determining the current performance of the material. A new concept is to introduce pre-formed ferromagnetic NPs into YBCO, which may induce additional sources of "ferromagnetic pinning".18 This would additionally allow the investigation of the interplay between superconductivity and ferromagnetism, which has been traditionally considered as an antagonistic phenomenon.19,20

There is currently much interest to develop hybrid YBCO nanocomposites with embedded ferrite NPs that can be prepared by means of Chemical Solution Deposition (CSD), an economically and industrially scalable method.21 For this application, the ex situ grown magnetic NPs must be stable in the highly ionic YBCO solution. In previous studies, we have reported the development of two methods, the solvothermal and microwave (MW) radiation assisted routes allowing the synthesis of ferrite $MFe_2O_4$22,23 and $Fe_3O_4$ NPs with a controllable size and shape,23 which can be dispersed in several polar media, in particular in the alcoholic solvent used for YBCO growth. The fine structure of high quality, spherical $MFe_2O_4$ (M = Mn, Fe, Co, Ni, Zn, Cu) NPs of size <5 nm prepared using these methods was reported in ref. 24.

The epitaxial growth of ex situ nanocomposite films onto single crystalline substrates starting from a colloidal preformed solution requires a thermal treatment involving temperatures up to 800 °C and 200 ppm of $O_2$, and an oxygenation process at an oxygen partial pressure of 1 atm.21,25 Such a stringent thermal process may have a strong influence on the structure, cation distribution and, thus, the final magnetic properties of the NPs.26 Therefore, it is important to understand its effect on the isolated $CoFe_2O_4$ NPs, prior to their stabilization inside the YBCO matrix.

Herein, we report on the effect of a thermal process, mimicking that required for the growth of hybrid YBCO nanocomposites, on $CoFe_2O_4$ NPs grown using the MW one-pot method. The NPs were characterized by powder X-Ray Diffraction (XRD), Scanning Transmission Electron Microscopy (STEM) and Electron Energy Loss Spectroscopy (EELS); the magnetic properties were investigated using SQUID magnetometry and X-ray Magnetic Circular Dichroism (XMCD). XMCD at the Fe and Co edges, combined with Multiplet

Ligand Field (LFM) simulations, allowed us to determine the cation site occupancy distribution, and quantify the evolution of the cation's moments and the total magnetic moment per formula unit of the NPs at different stages of the thermal process.

# Experimental section

## Samples

CoFe2O4 nanoparticles were synthesized following the microwave-assisted route previously described:22 0.64 mmol of iron(III) acetylacetonate (97%) [Fe(acac)3] was suspended together with 0.32 mMol of cobalt(II) acetylacetonate [Co(acac)2] to 12.5 ml of triethylene glycol (TREG) 99%. The solution was homogenized by using an ultrasound bath for 10 min. The initial red solution was transferred to a 35 ml specific microwave vial with a magnetic stirrer. Thus, the solution was quickly heated by microwave radiation (300 W, 2450 MHz) until 220 °C, keeping this temperature constant for 10 min. Then the solution was cooled naturally to room temperature.

After the synthesis, the $CoFe_2O_4$ nanoparticles were washed from the TREG solution by adding several times a mixture of ethylacetate : ethanol 4 : 1 (12.5 ml), and recovering the nanoparticles by magnetic precipitation. Finally, the $CoFe_2O_4$ NPs were redispersed in methanol anhydrous (25 mL), obtaining a 13 mMol black $CoFe_2O_4$ colloidal dispersion. Methanol solvent was preferred over ethanol, used in our previous work,[22] because the former would be more adequate for the ulterior growth of YBCO nanocomposites from trifluoracetate (TFA) precursor solutions.

In order to prepare YBCO films with embedded $CoFe_2O_4$ (using the same method we successfully used to grow other types of nanocomposites[21]), after depositing the colloidal solution onto a crystalline substrate, it would be necessary to subject the film to a thermal treatment, basically including two steps: a pyrolysis process, to eliminate the excess of organic content present in the solution, and a growth step, during which the YBCO thin film would be formed. So as to analyse the effect of the thermal process on the NPs, before embedding them in the YBCO matrix, we applied the same thermal process to as synthesized $CoFe_2O_4$ NPs (S1), and studied the NPs after the pyrolysis step (S2), at an intermediate stage during the growth process (quench, S3) and at the end of the growth-oxygenation process (S4), see Fig. 1.

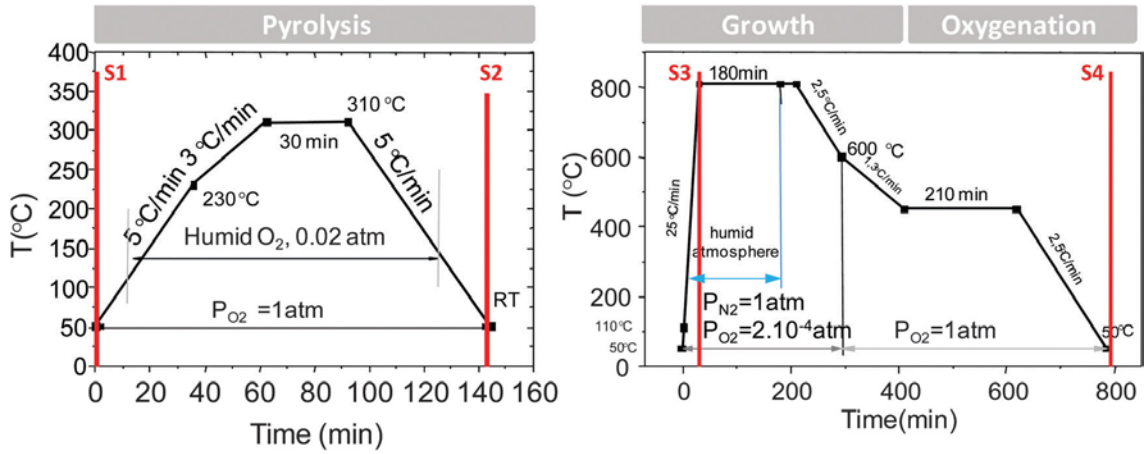


**Fig. 1** The NPs were subjected to the thermal treatment that would be required to generate YBCO + $CoFe_2O_4$nanocomposites by CSD. We studied NPs at 4 different states: as synthesized (S1), after the pyrolysis process (S2), after quenching at 800 °C (S3) and at the end of the growth-oxygenation process (S4).

## Characterization

**X-ray diffraction.** The crystallinity of the different NPs was verified by X-ray diffraction, using a Phillips XPert diffractometer equipped with two goniometers and a Cu tube. For the X-ray measurements the NPs were dried under a $N_2$ atmosphere until a powder was formed. This powder was subjected to the different processing conditions (pyrolysis, quenching and growth processes). After each step the powder was pulverized using a quartz mortar and then placed in a Si holder to place it in the equipment.

**STEM-EELS.** Scanning transmission electron microscopy observations were carried out in an aberration-corrected JEOL JEM-ARM200 CF, operated at 200 kV and equipped with a cold field emission gun and a Gatan quantum electron energy-loss spectrometer (EELS). The nanoparticles were dispersed on a holey carbon coated grid for electron microscopy observations.

**SQUID magnetometry.** Magnetic measurements were performed using a Quantum Design SQUID magnetometer equipped with a 9 T magnet. Zero-field-cooled (ZFC) and field-cooled (FC) magnetizations were recorded over the 5–300 K temperature range with an applied magnetic field of 50 Oe. *M*(*H*) cycles from −7 to 7 T, performed at 1.8 K and 300 K, were conducted after a ZFC process. Measurements were carried out on dried NPs (*ca.* 1 μm) immobilized in vacuum grease. Thermogravimetric analyses (TGA) were performed on NPs of the same batch to determine the percentage of the organic ligand remaining on the surface of the NPs (around 20% for the synthesized NPs).[22] Reported SQUID magnetic moments in emu $g^{-1}$ have been corrected for the amount of organic material, and are affected by a ~5% error.

**XAS & XMCD.** X-ray absorption spectroscopy (XAS) and X-ray magnetic circular dichroism (XMCD) experiments at the Fe and Co $L_{2,3}$ edges were performed at BOREAS beamline at ALBA Synchrotron in

Barcelona in Total Electron Yield (TEY) detection and a 100% circular polarization rate. The NPs were mounted on carbon tape attached to a copper sample holder. X-ray magnetic circular dichroism (XMCD) spectra were obtained at 300 K, 6 T as the difference between two XAS spectra with negative and positive helicities.

**LFM calculations.** XAS and XMCD spectra were simulated within the Ligand Field Multiplet (LFM) model using the CTM4XAS 5.0 program,[27] including spin–orbit coupling, crystal field (CF) effects and reduction of the Slater integrals F(dd), F(pd) and G(pd) to include the interatomic configuration interaction.

# Results

In this section, we present the structural and magnetic characterisation of the as synthesized $CoFe_2O_4$ NPs (S1), pyrolized NPs (S2), quenched NPs (S3) and NPs at the end of the growth and oxygenation process (S4).

## X-ray diffraction results

Fig. 2 shows the XRD patterns obtained from $CoFe_2O_4$ NPs at the four stages of the thermal process. All samples exhibited reflection peaks consistent with the spinel cubic structure of cobalt ferrite, according to the ICDD 04-016-3954 standard. After the quenching and growth processes, an overall narrowing of the individual diffraction peaks is observed, which is assigned to a coarsening of the NPs. The average crystallite sizes were calculated using Debye–Scherrer's equation applied to the most intense (311) diffraction peak, and found to be 4 nm (S1) and 5 nm (S2). For samples S3 and S4 the narrowness of the peak (311), similar to that expected for bulk material, hindered the application of the Debye–Scherrer's equation, so it can only be estimated that NP size is >100 nm.

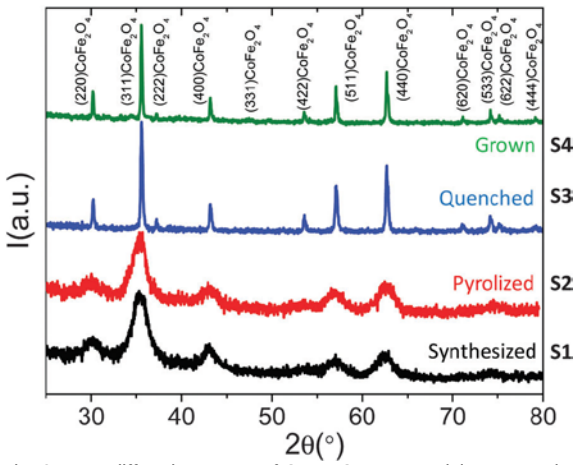


Fig. 2 X-ray diffraction scans of $CoFe_2O_4$ nanoparticles as synthesized (S1), pyrolized (S2), quenched (S3) and grown (S4).

## SQUID magnetometry results

The field-dependent magnetization of all the samples at $T$ = 1.8 K (Fig. 3a) displayed open $M(H)$ hysteresis loops, characteristic of ferromagnetic NPs. For the as synthesized NPs (S1), the saturation magnetization $M_s$ at 1.8 K was found to be 85.7 emu $g^{-1}$, close to the value of bulk cobalt ferrite, and the coercive field was $H_c \approx 8.3$ kOe. After the pyrolysis (S2), the saturation magnetization is reduced (61.3 emu $g^{-1}$) and the coercive field increases to $H_c$ = 15.6 kOe. However, after the quenching (S3) and at the end of the growth process (S4), the initial saturation magnetization values and coercive fields are recovered.

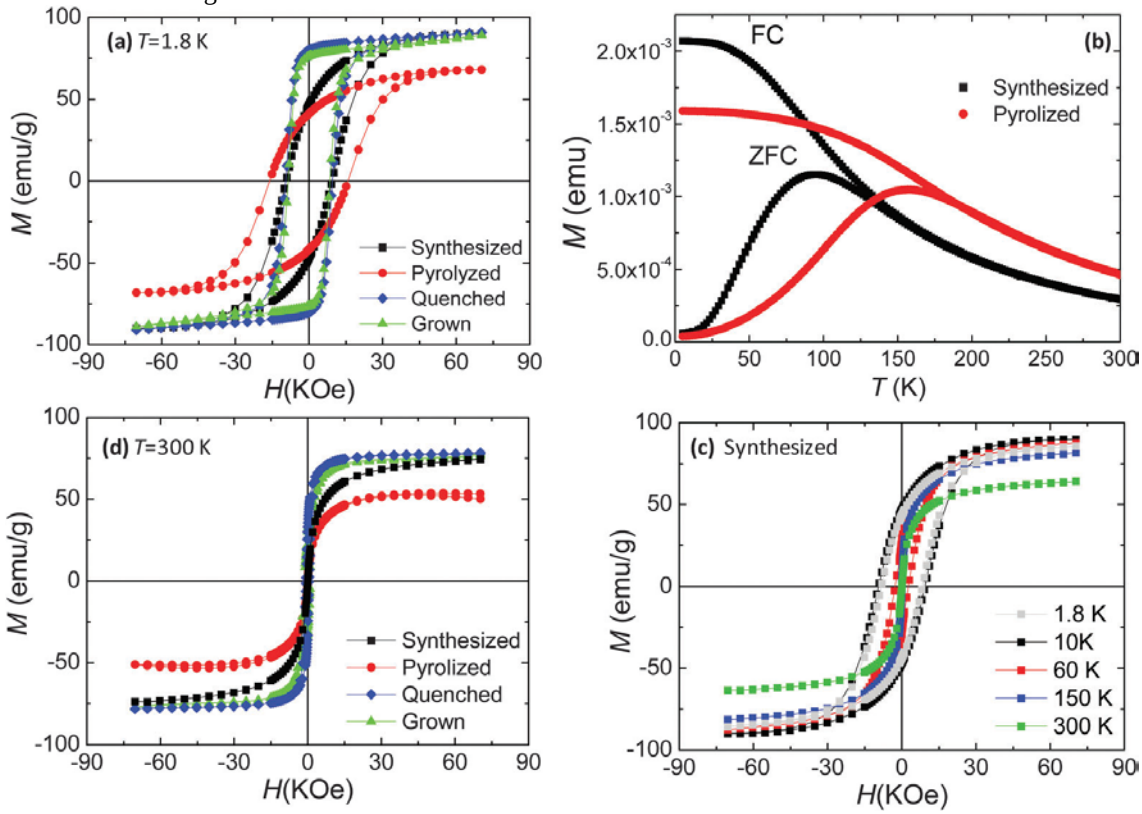


**Fig. 3** SQUID magnetometry measurements for the $CoFe_2O_4$ NPs at four stages of the thermal process. (a) Magnetization curves as a function of the applied magnetic field at 1.8 K (a) and 300 K (d); (b) FC and ZFC curves measured at 50 Oe; (c) isothermal $M(H)$ curves of the synthesized NPs.

Fig. 3b displays the FC/ZFC magnetization curves of synthesized (S1) and pyrolized NPs (S2) measured at 50 Oe, which are typical of small, dispersed superparamagnetic NPs. For S1 the peak temperature, $T_{max}$ = 95 K, is only somewhat below the crossing point between the two curves, signalling the blocking temperature $T_B$ = 120 K. In contrast, for the coarsened NPs S3 and S4 no blocking in the FC/ZFC was observed up to 300 K.

The isothermal $M(H)$ curves in Fig. 3c show the evolution from ferromagnetic to superparamagnetic behaviour across TB for the as synthesized NPs (S1). The saturation magnetization decreases only slightly, as expected for $CoFe_2O_4$ NPs, to ~75.3 emu $g^{-1}$ at 300 K.

The *M*(*H*) curves of all the NPs at 300 K are shown in Fig. 3d. The curves of the small sized NPs S1 and S2 NPs show superparamagnetic behaviour, while those of S3 and S4 preserve a small coercivity of 0.5 and 1 kOe, respectively.

The XRD and magnetometry results considered altogether seem to indicate that the pyrolysis process does not modify the NP size, but decreases the macroscopic saturation magnetization. The quenching and growth process produce significant NP coarsening, but good crystallinity is preserved, and the magnetization is bulk-like, similar to that of grown NPs.

## STEM-EELS results

Further insight into the NP size, structure and electronic distribution was obtained by STEM-EELS analysis (Fig. 4). The STEM images of the synthesized and pyrolized CoFe2O4 NPs, Fig. 4a and b, confirm the high crystalline quality, and the size of the NPs (4–6 nm) is in good agreement with XRD results. On the other hand, the significant coarsening of the NPs after the quenching and growth process is evidenced in Fig. 4c and d, respectively, as already observed by XRD.

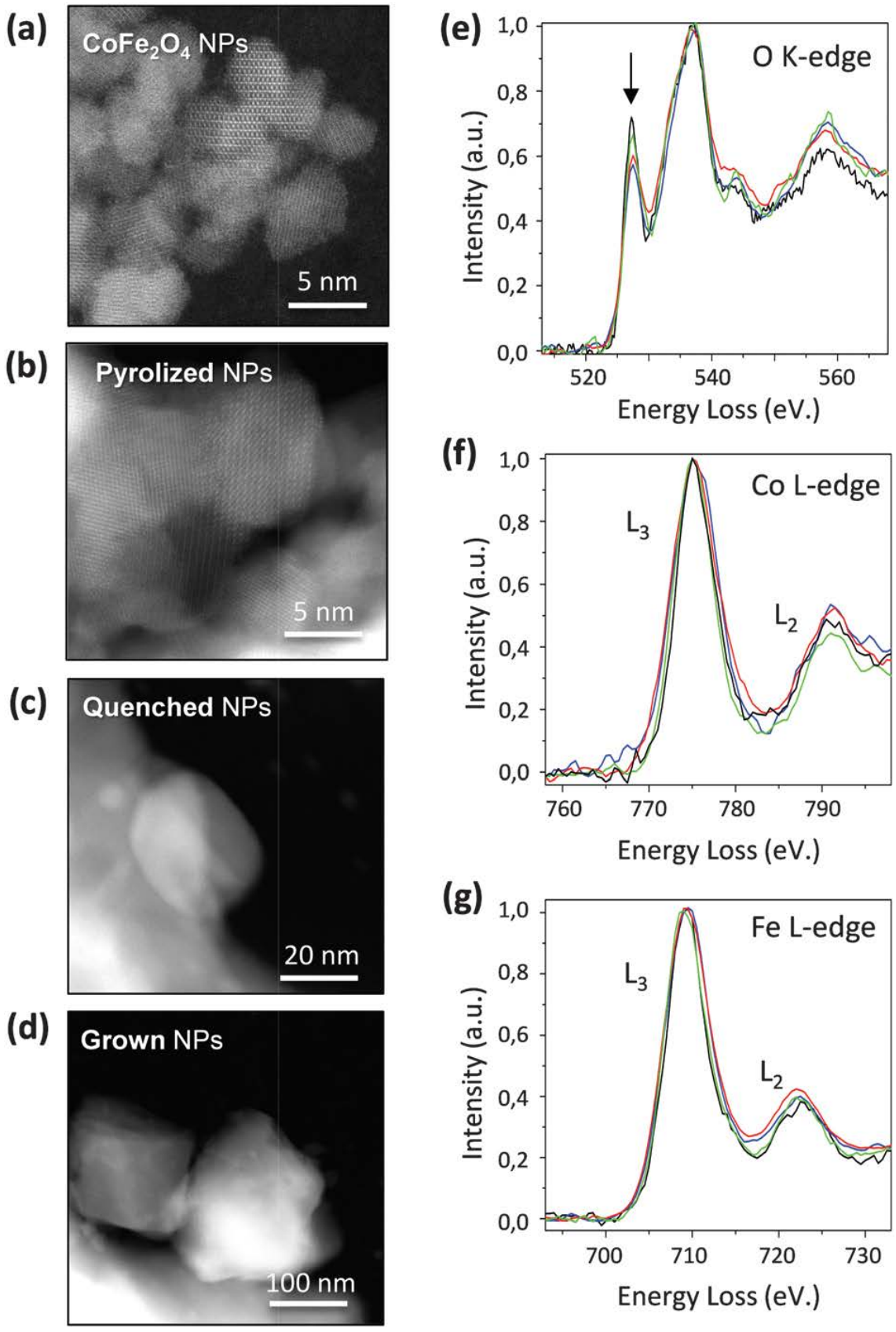


**Fig. 4** Left: STEM images of the (a) as synthesized $CoFe_2O_4$ NPs, (b) pyrolized NPs, (c) quenched NPs and (d) grown NPs. Right: (e) EEL O K-edge (the arrow signals the pre-peak, at the onset of the edge, centred at 527 eV), (f) Co L-edge and (g) Fe L-edge of the $CoFe_2O_4$ NPs in the 4 stages: as synthesized (in black), pyrolized (in red), quenched (in blue) and grown (in green).

Fig. 4e–g show the EEL O K-edge, Co L-edge and Fe L-edge spectra, respectively, of the S1 to S4 NPs. The $L_2(L_3)$ features in the metal spectra arise from $2p_{1/2}(2p_{3/2}) \rightarrow 3d$ transitions, while the O K-edge comes from transitions from the oxygen $1s \rightarrow 2p$ states, which are hybridized with Fe 3d (Co 3d) orbitals due to covalent Fe–O (Co–O) bonding. In bulk iron oxides, it has been demonstrated that the intensity of the pre-peak in the O K-edge (normalized to the main peak) and the intensity ratio of the Fe $L_2$ and $L_3$ white lines ($L_{23}$ ratio) increase with the iron oxidation state[28–30] although the quantitative determination of the valence is difficult. Conversely, for Co the oxidation state decreases with the L23 ratio.[31,32]

Fig. 4e shows the comparison of the O K-edge features of all studied NPs. Notice that the signal from the synthesized S1 and grown S4 NPs (in black and green, respectively) presents a higher pre-peak intensity compared to the one from the pyrolized S2 and quenched S3 (in red and blue, respectively).

Co and Fe L-edges also show differences between the $CoFe_2O_4$ NPs, Fig. 4f and g, respectively. The Fe and Co L2 peaks of the synthesized S1 and grown S4 NPs (in black and green, respectively) have lower intensity than those from the pyrolized S2 and quenched S3 ones (in red and blue, respectively).

All these changes can be quantified. In the case of the O K-edge peak, the normalized O K pre-peak intensity has been used to quantify these changes. To do so, Gaussian curves are fitted to both the pre-peak and the main peak.[33] In Fig. 5a, we present the values of the O K-edge normalised pre-peak intensity, showing that the pyrolized and quenched NPs were reduced when subjected to those thermal processes.

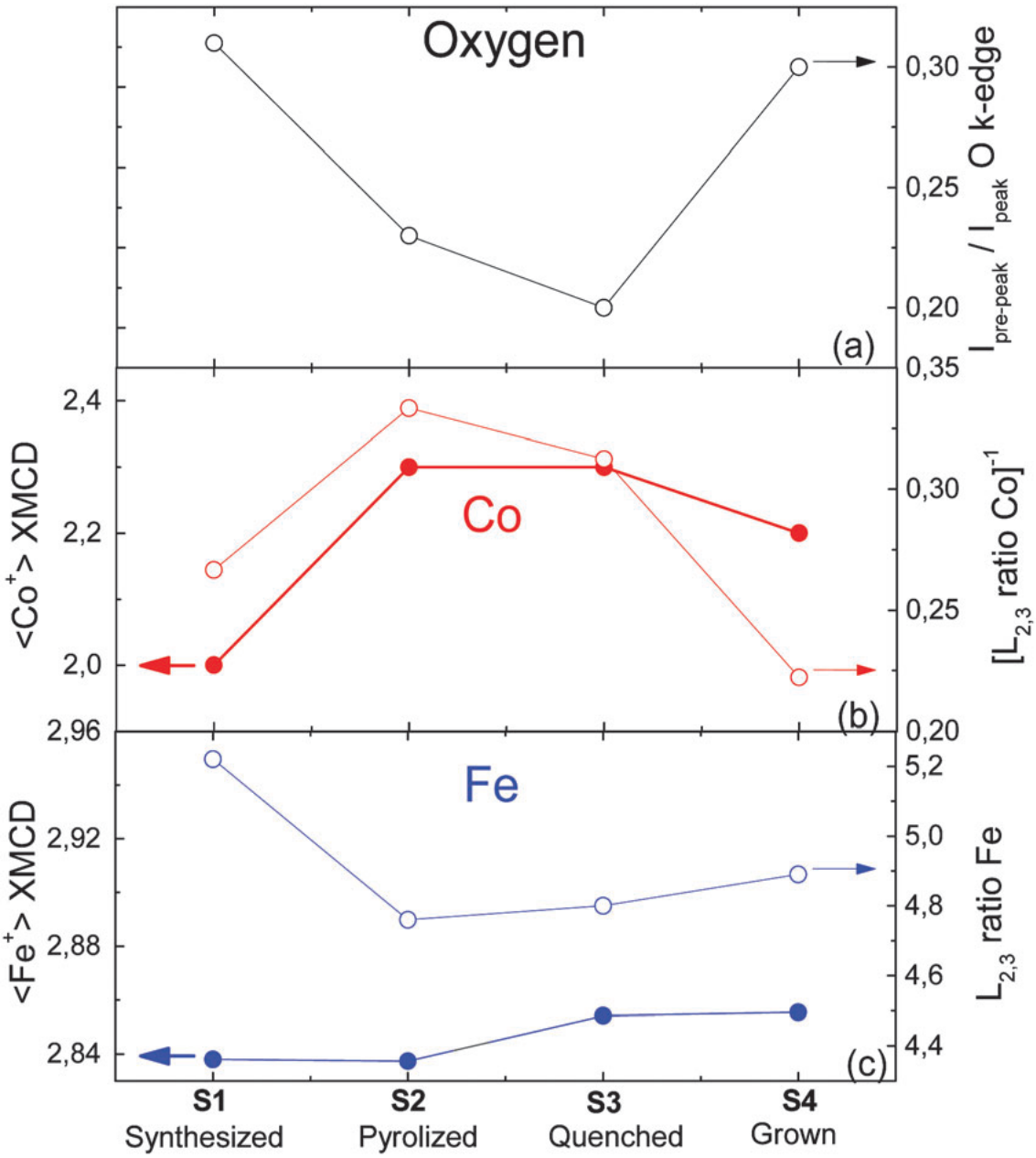


**Fig. 5** Evolution of the oxygen contents and Co, Fe valences through the thermal process, as obtained from EELS (open symbols) and XMCD (bold symbols). (a) Normalised intensity of the O K pre-peak from EELS; (b) left scale: average $\langle Co^{+} \rangle$ from XMCD; right: inverse of the $L_{23}$ ratio from Co L-edge EEL, correlated with the Co valence; (c) left: average $\langle Fe^{+} \rangle$ from XMCD; right: $L_{23}$ ratio from Fe L-edge EEL, directly related to the Fe valence.

For Fe and Co L-edges we have used the so-called 2nd derivative method to obtain the L2,3 ratios,34Fig. 5b and c. The evolution of the Fe L2,3 ratio, following the same trend as the O K-edge, shows that in the pyrolized and quenched NPs iron has reduced; in contrast Co at those stages has oxidised.

## XAS & XMCD results

X-ray absorption (XAS) and magnetic circular dichroism (XMCD) measurements at the Fe $L_{2,3}$ and Co $L_{2,3}$ edges were performed to gain insight into the oxidation state and site occupancy of the Fe and Co atoms in the NPs at the four different thermal process stages S1–S4. Measurements were carried out at 300 K at a magnetic field of 6 T at which NPs are well saturated.

Fig. 6a shows the first results at the Fe L2,3 edge. The XAS & XMCD spectra present the typical aspect previously described for the Fe L2,3 edge of CoFe2O4.12,15,35 The XMCD at the L3 edge shows three characteristic peaks, each arising predominantly from an oxidation state/site of Fe in the structure: the lowest energy, negative peak corresponds to octahedral Fe2+Oh (and Fe3+Oh), the positive peak to tetrahedral Fe3+Td and the highest, negative peak to Fe3+Oh.

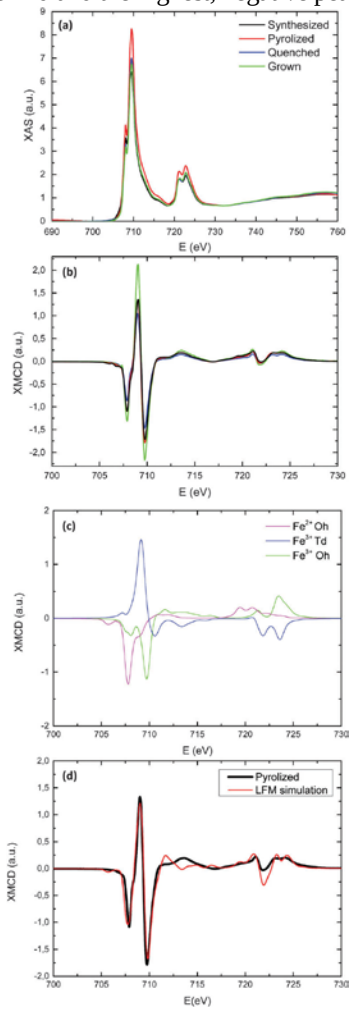


**Fig. 6** (a) XAS and (b) XMCD spectra at the Fe $L_{2,3}$ edge of synthesized, pyrolized, quenched and grown $CoFe_2O_4$ NPs; (c) LFM calculated XMCD spectra for $Fe^{2+}$Oh, $Fe^{3+}$Td and $Fe^{3+}$Oh; (d) experimental XMCD data for the pyrolized $CoFe_2O_4$ NPs (black) and the fit using LFM calculations (red).

To quantify the cation distribution over the three Fe sites, the experimental XMCD of each sample was fitted using a linear combination of the LFM calculated spectra for each site. For these simulations, we used parameters close to those described in ref. 12: the CF parameters were 10Dq = 1.5 eV, 1.2 eV, −0.6 eV for Fe3+Oh, Fe2+Oh, Fe3+Td, respectively; a Slater reduction of 70%, 80%, 75% was used to F(dd), F(pd) and G(pd). The results were convoluted by a Lorentzian of $\Gamma$ = 0.3(0.5) eV for the $L_3$($L_2$) edge to account for intrinsic core-hole lifetime broadening, and by a Gaussian of $\sigma$ = 0.2 eV to account for instrumental broadening.

As an example, we show the LFM calculated XMCD spectra for Fe2+Oh, Fe3+Td and Fe3+Oh cations (Fig. 6c) and the fit of the experimental XMCD with a linear combination of the three (Fig. 6d), for the pyrolized NPs. The determined Fe cation distribution for all studied samples is summarized in Table 1.

**Table 1** Fe and Co site occupancies (in number of atoms) in $CoFe_2O_4$ NPs determined by fitting XAS & XMCD spectra using crystal field atomic multiplet calculations; last column: oxygen deficiency ($\delta$) per formula $CoFe_2O_{4-\delta}$

| | $Fe^{2+}O_h$ | $Fe^{3+}T_d$ | $Fe^{3+}O_h$ | $Fe^{2+}/Fe^{3+}$ | $Co^{2+}O_h$ | $Co^{2+}T_d$ | $Co^{3+}O_h$ | $Co^{3+}T_d$ | $Co^{2+}/Co^{3+}$ | $\delta$ (O) |
|---|---|---|---|---|---|---|---|---|---|---|
| S1 Synthesized | 0.32 | 0.75 | 0.93 | 0.19 | 0.97 | 0.03 | 0 | 0 | ∞ | 0.15 |
| S2 Pyrolized | 0.32 | 0.75 | 0.93 | 0.19 | 0.68 | 0.02 | 0.18 | 0.12 | 2.3 | 0.01 |
| S3 Quenched | 0.29 | 0.75 | 0.96 | 0.17 | 0.70 | 0 | 0.14 | 0.16 | 2.3 | 0.00 |
| S4 Grown | 0.29 | 0.84 | 0.87 | 0.18 | 0.80 | 0 | 0.10 | 0.1 | 4.0 | 0.05 |

We turn now to the results at the Co L2,3 edge (Fig. 7). The XAS & XMCD spectra (Fig. 7a, left and right) notably change from S1 to S4. This is especially clear looking at the fine structure of the L3 XAS and the asymmetry of the L2 XAS peak. For synthesized NPs, the L3 XAS peak shows a high intensity, twined peak (777.6, 779.9 eV) and a lower peak at higher energy (780.7 eV). In contrast, in the pyrolized and quenched NPs (S2 and S3), these two peaks have a similar intensity. Notice that for grown NPs S4 the spectra look more similar to that of synthesized NPs S1.

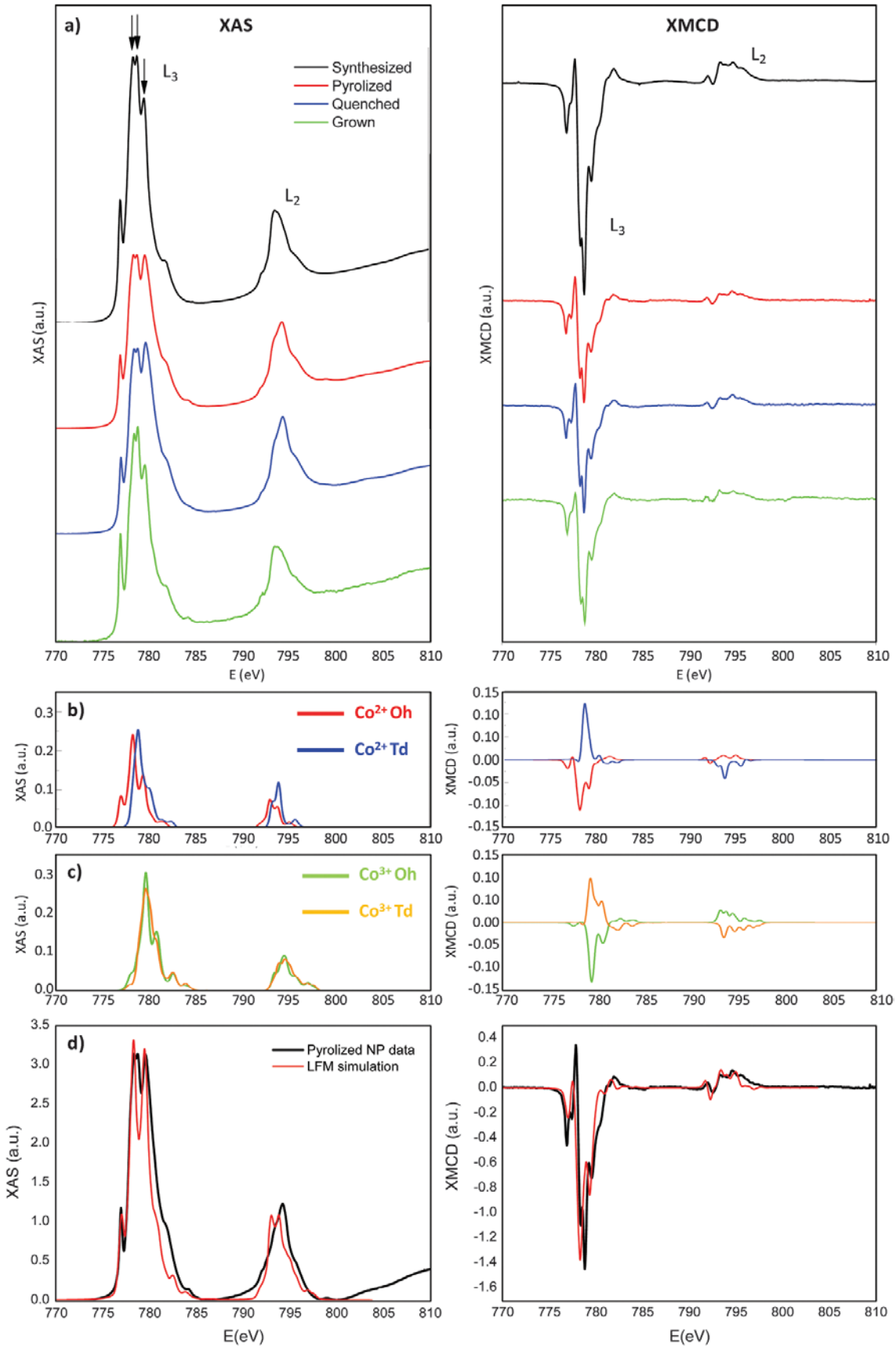


**Fig. 7** (a) (left) XAS and (right) XMCD spectra at the Co $L_{2,3}$ edge of the synthesized, pyrolized, quenched and grown $CoFe_2O_4$NPs; (b) LFM calculated XAS & XMCD spectra for $Co^{2+}$ in octahedral (Oh)

and tetrahedral (Td) coordination; (c) LFM calculated XAS & XMCD spectra for $Co^{3+}$ Oh and $Co^{3+}$ Td; (d) the background subtracted XAS & XMCD spectra for pyrolized NP and LFM fits.

These changes can be explained by differences in the Co cation distribution. Indeed, the site occupancy and the oxidation state of Co were deduced by fitting the XAS & XMCD experimental spectra with a linear combination of the LFM calculated spectra for $Co^{2+}$Oh, $Co^{2+}$Td, $Co^{3+}$ Oh and $Co^{3+}$Td. In this case, following ref. 36, the 2p and 3d spin–orbit interactions were reduced by multiplying by factors 0.98 and 0.75; a Slater reduction of 70%, 80% and 75% was considered for F(dd), F(pd) and G(pd), respectively; CF parameters were 1.2 eV (−0.6 eV) for Oh(Td) Co sites; and Lorentzian and Gaussian broadening was $\Gamma$ = 0.1(0.3) eV for $L_3(L_2)$ and $\sigma$ = 0.2 eV.

Table 1 summarizes the Co cation distribution found for all NPs. The spectra of synthesized NPs S1 resemble that of previously reported $CoFe_2O_4$ spinels,14,15,35,37 and correspond to a major distribution of cations in $Co^{2+}$Oh sites (97%) and a minor fraction in $Co^{2+}$Td sites (3%). In contrast, to account for the experimental data of NPs in the three late heating stages, an additional contribution of $Co^{3+}$ cations had to be necessarily included. For example, Fig. 7d shows the fit of the pyrolized NP (S2) XAS & XMCD data using a linear combination of the four LFM calculated Co2+Oh, Co2+Td, Co3+Oh and Co3+Td spectra, depicted in Fig. 7b and c.

Table 1 summarizes the site occupancy for Fe and Co atoms found for all the NPs. For the synthesized NPs S1, the cation distribution is similar to that reported for one-pot synthesized $CoFe_2O_4$ NPs from bimetallic pivalate clusters.[15] On the other hand, the cation occupancies found for S1 in this work are somewhat different (the %Fe/Co Td ratio is larger) than those found by neutron diffraction[24] for NPs prepared by the MW route and stabilized in ethanol,[22] which had a ~20% smaller magnetic moment per formula unit. TREG aging causes the generation of different length polyol chains,38 something that could justify the cationic distribution differences found.

Using the table's occupancies, the average iron and cobalt oxidation states, $\langle Fe^{+} \rangle$ and $\langle Co^{+} \rangle$, have been determined for each sample. The evolution of these average valences through the thermal process is depicted Fig. 5b and c. Cobalt is oxidised at stages S2 and S3, but is reduced almost to its initial value after stage S4, whereas iron follows the converse process. If the general formula for the NPs is written as:

$$(Co_{Oh}^{2+})_x(Co_{Td}^{2+})_y(Co_{Oh}^{3+})_z(Co_{Td}^{3+})_w(Fe_{Oh}^{2+})_l(Fe_{Td}^{3+})_m(Fe_{Oh}^{3+})_nO_{4-\delta},$$

where the ratio Co : Fe is 1 : 2, $(l + m + n) = 2(x + y + z + w)$, it is verified that the charge equilibrium holds in every case, *i.e.* $2(x + y + l) + 3(z + w + m + n) = 2(4 - \delta)$, with $\delta < 0.15$.

The sum rules39,40 were applied to determine the orbital ($m_L$), spin ($m_S$), and the total magnetic moment ($m_L + m_S$) per average Fe ion ($m_{Fe}$) and Co ion ($m_{Co}$) from the XAS and XMCD spectra. The number of holes $n_h$ per average metal ion M was estimated considering the relative distribution of cations derived from the simulations:

$$n_h = n_h(M^{2+})\cdot(\%M^{2+}) + n_h(M^{3+})\cdot(\%M^{3+})$$

The number of holes per specific cation was calculated as $n_h = 10 - n_{3d}$, where $n_{3d}$ was taken as 5.3 and 6.1 for $Fe^{3+}$ and $Fe^{2+}$cations, respectively (from Fe 3p core-level photoemission) and 7.21 for $Co^{2+}$ and 6.5 for $Co^{3+}$ (as expected for CoO[41] and a high spin $Co^{3+}$ oxide[42]). We emphasize here that the magnetic moments obtained from the XMCD sum rules give the "averaged" magnetic moments per cation within the ferrite sample formula unit, *i.e.*, the antiferromagnetic alignment, non-ideal spinel inversion, and variations in cation valences are inherent to the resulting numbers and thus lower than the expected ionic values per cation.

Fig. 8a summarizes the mS and mL magnetic moments found for Fe and Co ions, for the NPs at thermal stages S1–S4. For the synthesized NPs (S1), Co spin and orbital magnetic moments (mS = 0.8 μB, mL = 0.3 μB) are close to values earlier reported for CoFe2O4 films;36 the Fe orbital magnetic moment is mL ≈ 0, as expected,43 whereas the spin moment is in the upper range of previously reported values.20 Upon the application of the thermal process, iron's orbital magnetic moment is practically unchanged, mL ≈ 0 within the error; in contrast, mS(Fe), mS(Co) and mL(Co) decrease after the pyrolysis, but recover at the end of the growth process.

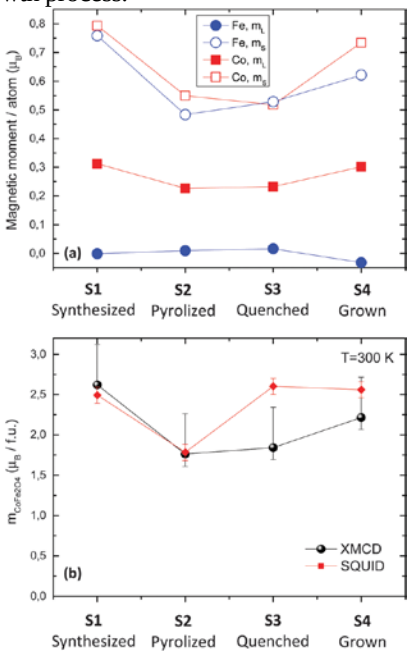

**Fig. 8** (a) Orbital and spin magnetic moments per Co and Fe cations in the $CoFe_2O_4$ NPs at the 4 different studied stages; (b) comparison of the magnetic moment per formula unit at 300 K as determined from SQUID magnetometry, and from XMCD applying sum rules (the corresponding error bar has been estimated considering the inaccuracy of sum rules for transition-metal L edges, as given in ref. 44)

The magnetic moment per unit formula as determined from XMCD was quantified as[35] $m_{CoFe_2O_4} = 2m_{Fe} + mCo$. Fig. 8b compares the XMCD determined $m_{CoFe_2O_4}$ with the value determined from SQUID magnetometry (in $\mu_B$/f.u.), at the same temperature. For the interpretation of the results, it should be reminded that XMCD in the TEY detection mode is just sensitive to the first ~6 nm of sample, whereas SQUID magnetometry is a macroscopic measurement. In the synthesized (S1) and pyrolized (S2) stages the NPs are <5 nm; in this case XMCD and SQUID obtained $m_{CoFe_2O_4}$ values are coincident within the error, as both represent the average magnetic moment per unit formula of the whole NP. The decrease in $m_{CoFe_2O_4}$ after the pyrolysis is similarly observed by both techniques.

In contrast, after the quenching (S3) and growth (S4) processes, the NP's size is >100 nm, according to XRD. Therefore, the XMCD determined $m_{CoFe_2O_4}$ value corresponds mainly to the surface, whereas the SQUID $m_{CoFe_2O_4}$ value is majorly due to the core contribution. As shown in Fig. 8b, at stages S3 and S4 the $m_{CoFe_2O_4}$ values found by XMCD are smaller than those obtained by SQUID, indicating that the thermal process has mainly affected the NPs' surface.

# Conclusions

High quality $CoFe_2O_4$ nanoparticles were synthesized by a one-pot, microwave-radiation assisted route, allowing their dispersion in an alcoholic solvent, as necessary for the preparation of YBCO nanocomposites by Chemical Solution Deposition. The growth of hybrid films using this method would require subjecting the sample to a thermal process involving stringent temperature and oxygen pressure conditions. In this work, we have investigated how this thermal process affects the structure and magnetic properties of the nanoparticles alone, by combining different techniques: X-Ray Diffraction (XRD), Superconducting Quantum Interference Device magnetometry (SQUID), Scanning Tunneling Electron Microscopy (STEM), Electron Energy Loss Spectroscopy (EELS) and X-ray magnetic circular dichroism (XMCD). Results have allowed us to draw the following conclusions:

The synthesized nanoparticles (S1) have small sizes (4 nm) and high crystallinity, as shown by STEM and XRD; they display high macroscopic saturation magnetization (85.7 emu $g^{-1}$) at 1.8 K and are superparamagnetic at room temperature.

After the pyrolysis process (S2), the nanoparticle size remains unchanged (5 nm, XRD results). A 30% decrease of the saturation magnetization is observed, which is associated with the oxidation of a fraction of $Co^{2+}$ ions to $Co^{3+}$, and the concomitant increasing occupation of Td sites by Co atoms.

In the subsequent step, the nanoparticles are heated at a high rate (25 °C $min^{-1}$) to a high temperature (800 °C) under low oxygen partial pressure. This process results in a major coarsening of the nanoparticles (>100 nm) quenched at this stage (S3), as evidenced from XRD peak narrowing, and the NPs are no longer superparamagnetic at room temperature. The surface of the NPs still contains oxidized Co ions, as evidenced from XMCD measurements in Total Electron Yield, only sensitive to the outermost 6 nm shell. However, the SQUID macroscopic magnetic saturation, dominated by the major core contribution, displays a bulk, recovered value.

In the subsequent step of the thermal process, the temperature is decreased to 420 °C and the NPs are subjected to an $O_2$pressure of 1 atm for a long time (~500'). The grown nanoparticles (S4) present Fe(Co) surface atoms oxidized (reduced) compared to the previous stage, however the overall macroscopic saturation magnetization $M_s$ is as high as that of the synthesized nanoparticles. The decreasing contribution from the surface shell with increasing particle size results in high values of $M_s$ at the highest calcining temperatures. Similar size effects in $CoFe_2O_4$ nanoparticles have earlier been reported.45–48

In conclusion, we have demonstrated the magnetic stability of the $CoFe_2O_4$ nanoparticles against the thermal process needed for the preparation of YBCO nanocomposites. This result paves the way for the flexible, low-cost fabrication by chemical-solution methods of flexible, low cost hybrid YBCO superconducting films with *ex situ* grown ferromagnetic nanoparticles.

# Acknowledgements

Authors acknowledge the MICIN (NANOSELECT, CSD2007-00041 and MAT2014-51778-C2-1-R and FEDER), Generalitat de Catalunya (2014SGR 753 and Xarmae), "Severo Ochoa" Programme for Centres of Excellence in R&D (SEV-2015-0496), the CONSOLIDER Excellence Network (MAT2015-68994-REDC) and the EU (EU-FP7 NMP-LA-2012-280432 EUROTAPES project). Electron microscopy performed at the Centro Nacional de Microscopía Electrónica (UCM) was sponsored by the ERC Starting Investigator Award No. STEMOX#239739. J. G. and M. C. also acknowledge the Ramon y Cajal program (RYC-2012-11709,

RYC-2013-12448). The XMCD experiments were performed at the BOREAS beamline of the ALBA Synchrotron Light Facility with the collaboration of ALBA staff.

# References


1. M. Sugimoto, *J. Am. Ceram. Soc.*, 2004, **82**, 269–280.
2. M. Sivakumar, S. Kanagesan, R. Suresh Babu, S. Jesurani, R. Velmurugan, C. Thirupathi and T. Kalaivani, *J. Mater. Sci.: Mater. Electron.*, 2012, **23**, 1045–1049.
3. C. W. Jung and P. Jacobs, *Magn. Reson. Imaging*, 1995, **13**, 661–674.
4. C. V. G. Reddy and S. V Manorama, *J. Electrochem. Soc.*, 2000, **147**, 390–393.
5. L. Zhao, H. Zhang, Y. Xing, S. Song, S. Yu, W. Shi, X. Guo, J. Yang, Y. Lei and F. Cao, *J. Solid State Chem.*, 2008, **181**, 245–252.
6. L. Chen, Y. Shen and J. Bai, *Mater. Lett.*, 2009, **63**, 1099–1101 .
7. P. Lavela and J. L. Tirado, *J. Power Sources*, 2007, **172**, 379–387.
8. K. Maaz, S. Karim, A. Mumtaz, S. K. Hasanain, J. Liu and J. L. Duan, *J. Magn. Magn. Mater.*, 2009, **321**, 1838–1842.
9. Y. Zhang, Z. Yang, D. Yin, Y. Liu, C. Fei, R. Xiong, J. Shi and G. Yang, *J. Magn. Magn. Mater.*, 2010, **322**, 3470–3475.
10. J. Ma, J. Zhao, W. Li, S. Zhang, Z. Tian and S. Basov, *Mater. Res. Bull.*, 2013, **48**, 214–217.
11. S. Yáñer-Vilar, M. Sánchez-Andújar, C. Gómez-Aguirre, J. Mira, M. A. Señaris-Rodríguez and S. Castro-García, *J. Solid State Chem.*, 2009, **182**, 2685–2690 .
12. W. Baaziz, B. P. Pichon, Y. Liu, J.-M. Greneche, C. Ulhaq-Bouillet, E. Terrier, N. Bergeard, V. Halté, C. Boeglin, F. Choueikani, M. Toumi, T. Mhiri and S. Begin-Colin, *Chem. Mater.*, 2014, **26**, 5063–5073.
13. E. Manova, B. Kunev, D. Paneva, I. Mitov, L. Petrov, C. Estournès, C. D'Orléans, J. L. Rehspringer and M. Kurmoo, *Chem. Mater.*, 2004, **16**, 5689–5696.
14. V. S. Coker, N. D. Telling, G. Van Der Laan, R. a D. Pattrick, C. I. Pearce, E. Arenholz, F. Tuna, R. E. P. Winpenny and J. R. Lloyd,*ACS Nano*, 2009, **3**, 1922–1928 .
15. K. O. Abdulwahab, M. A. Malik, P. O'Brien, G. A. Timco, F. Tuna, C. A. Muryn, R. E. P. Winpenny, R. A. D. Pattrick, V. S. Coker and E. Arenholz, *Chem. Mater.*, 2014, **26**, 999–1013.
16. J. Gutiérrez, A. Llordés, J. Gázquez, M. Gibert, N. Romà, S. Ricart, A. Pomar, F. Sandiumenge, N. Mestres, T. Puig and X. Obradors, *Nat. Mater.*, 2007, **6**, 367–373.
17. A. Llordés, A. Palau, J. Gázquez, M. Coll, R. Vlad, A. Pomar, J. Arbiol, R. Guzmán, S. Ye, V. Rouco, F. Sandiumenge, S. Ricart, T. Puig, M. Varela, D. Chateigner, J. Vanacken, J. Gutiérrez, V. Moshchalkov, G. Deutscher, C. Magen and X. Obradors, *Nat. Mater.*, 2012, **11**, 329–336.
18. L. N. Bulaevskii, E. M. Chudnovsky and M. P. Maley, *Appl. Phys. Lett.*, 2000, **76**, 2594–2596.
19. V. L. Ginzburg, *Sov. Phys. – JETP*, 1957, **4**, 153.
20. F. Lévy, I. Sheikin, B. Grenier, C. Marcenat and A. Huxley, *J. Phys.: Condens. Matter*, 2009, **21**, 164211 .
21. P. Cayado, K. De Keukeleere, A. Garzón, L. Perez-Mirabet, A. Meledin, J. De Roo, F. Vallés, B. Mundet, H. Rijckaert, G. Pollefeyt, M. Coll, S. Ricart, A. Palau, J. Gázquez, J. Ros, G. Van Tendeloo, I. Van Driessche, T. Puig and X. Obradors,*Supercond. Sci. Technol.*, 2015, **28**, 124007.
22. E. Solano, L. Perez-Mirabet, F. Martinez-Julian, R. Guzmán, J. Arbiol, T. Puig, X. Obradors, R. Yañez, A. Pomar, S. Ricart and J. Ros, *J. Nanopart. Res.*, 2012, **14**, 1034 .
23. A. Garzón-Manjón, E. Solano, M. de la Mata, R. Guzmán, J. Arbiol, T. Puig, X. Obradors, R. Yáñez, S. Ricart and J. Ros, *J. Nanopart. Res.*, 2015, **17**, 291 .
24. E. Solano, C. Frontera, T. Puig, X. Obradors, S. Ricart and J. Ros, *J. Appl. Crystallogr.*, 2014, **47**, 414–420 .
25. X. Obradors, T. Puig, A. Pomar, F. Sandiumenge, N. Mestres, M. Coll, A. Cavallaro, N. Roma, J. Gazquez, J. C. Gonzalez, O. Castano, J. Gutierrez, A. Palau, K. Zalamova, S. Morlens, A. Hassini, M. Gibert, S. Ricart, J. M. Moreto, S. Pinol, D. Isfort and J. Bock, *Supercond. Sci. Technol.*, 2006, **19**, S13–S26 .
26. Q. Cao, Z. Liu and R. Che, *New J. Chem.*, 2014, **38**, 3193–3198 .
27. E. Stavitski and F. M. F. de Groot, *Micron*, 2010, **41**, 687–694.
28. C. Colliex, T. Manoubi and C. Ortiz, *Phys. Rev. B: Condens. Matter Mater. Phys.*, 1991, **44**, 11402–11411.
29. M. Varela, J. Gázquez and S. J. Pennycook, *MRS Bull.*, 2012, **37**, 29–35.
30. H. K. Schmidt and W. Meder, *Micron*, 2006, **37**, 426 .

31. Z. L. Wang, *J. Appl. Phys.*, 1997, **70**, 3362.
32. Z. L. Wang, *J. Phys. Chem. B*, 1997, **101**, 35.
33. M. Varela, M. Oxley, W. Luo, J. Tao, M. Watanabe, a. Lupini, S. Pantelides and S. Pennycook, *Phys. Rev. B: Condens. Matter Mater. Phys.*, 2009, **79**, 085117.
34. G. A. Botton, C. C. APPEL, A. Horsewell and W. M. Stobbs, *J. Microsc.*, 1995, **180**, 211–216.
35. V. S. Coker, C. I. Pearce, R. a D. Pattrick, G. Van Der Laan, N. D. Telling, J. M. Charnock, E. Arenholz and J. R. LLoyd, *Am. Mineral.*, 2008, **93**, 1119–1132.
36. J. Moyer, C. a. Vaz, D. Arena, D. Kumah, E. Negusse and V. Henrich, *Phys. Rev. B: Condens. Matter Mater. Phys.*, 2011, **84**, 054447.
37. B. Y. Wang, H. T. Wang, S. B. Singh, Y. C. Shao, Y. F. Wang, C. H. Chuan, P. H. Yeh, J. W. Chiou, C. W. Pao, H. M. Tsai, H. J. Lin, J. F. Lee, C. Y. Tsai, W. F. Hsieh, M.-H. Tsai and W. F. Pong, *RSC Adv.*, 2013, **3**, 7884.
38. S. N. Rishikeshi, S. S. Joshi, M. K. Temgire and J. R. Bellare, *Dalton Trans.*, 2013, **42**, 5430–5438.
39. B. Thole, P. Carra, F. Sette and G. van der Laan, *Phys. Rev. Lett.*, 1992, **68**, 1943–1946.
40. P. Carra, B. T. Thole, M. Altarelli and X. Wang, *Phys. Rev. Lett.*, 1993, **70**, 694–697.
41. G. van der Laan, E. Arenholz, R. V Chopdekar and Y. Suzuki, *Phys. Rev. B: Condens. Matter Mater. Phys.*, 2008, **77**, 64407.
42. T. Saitoh, T. Mizokawa, a. Fujimori, M. Abbate, Y. Takeda and M. Takano, *Phys. Rev. B: Condens. Matter Mater. Phys.*, 1997,**55**, 4257–4266.
43. E. Goering, S. Gold, M. Lafkioti and G. Schuetz, *Europhys. Lett.*, 2005, **73**, 97–103
44. C. Piamonteze, P. Miedema and F. M. F. De Groot, *Phys. Rev. B: Condens. Matter Mater. Phys.*, 2009, **80**, 1–12.
45. E. Swatsitang, S. Phokha, S. Hunpratub, B. Usher, A. Bootchanont, S. Maensiri and P. Chindaprasirt, *J. Alloys Compd.*, 2016,**664**, 792–797 .
46. P. Laokul, S. Arthan, S. Maensiri and E. Swatsitang, *J. Supercond. Nov. Magn.*, 2015, **28**, 2483–2489
47. M. P. Gonzalez-Sandoval, A. M. Beesley, M. Miki-Yoshida, L. Fuentes-Cobas and J. A. Matutes-Aquino, *J. Alloys Compd.*, 2004, **369**, 190–194 .
48. M. Rajendran, R. C. Pullar, A. K. Bhattacharya, D. Das, S. N. Chintalapudi and C. K. Majumdar, *J. Magn. Magn. Mater.*, 2001,**232**, 71–83 .